Ultrafast Electronic and Structural Dynamics in Oxygen Evolution Reaction Catalysts

Emily Sprague-Klein,[‡] Brian T. Phelan,[∫] Michael Mara,[‡] Jin Yu,[|] Matt Drummer,[ϱ] Xiang He,[∫] Ksenija Glusac,[‡ϱ] Sungsik Lee,[|] Benjamin Reinhart,[|] Xiaoyi Zhang,[|] David M. Tiede,[∫] Lin X. Chen[‡*]

[∫] Chemical Sciences and Engineering Division, Argonne National Laboratory, Lemont IL 60439.

[‡] Department of Chemistry, Northwestern University, Evanston IL 60201 USA.

[ϱ] Department of Chemistry, University of Illinois Chicago IL 60607 USA.

[|] X-ray Science Division, Argonne National Laboratory, Lemont IL 60439.

***Corresponding author.** Email: l-chen@northwestern.edu

ABSTRACT: We investigate the ultrafast electronic and thermal properties of the bulk amorphous cobalt oxide water oxidation catalysts cobalt-phosphate (CoPi) and cobalt-borate (CoBi) using optical pump/X-ray probe correlated with *in situ* electrochemical transient absorption spectroscopy. The electronic signature of a light generated intermediate species is compared to steady-state *in situ* heating X-ray absorption spectroscopy (XAS) suggestive of non-thermal contributions to charge transfer formation on ultrafast timescales. With Co K-edge transient absorption spectroscopy, we observe a net photoreduction following 400 nm excitation that also initiates a potential-dependent increase in the excited-state fraction of trapped charge carriers that persists on nanosecond to microsecond timescales and is identified as a potential precursor state to oxygen evolving reactions (OER). Distinctly, the formation of excited-state species cannot be fully explained by photothermal reaction dynamics alone with potential contributions from electronic motion acting in concert with macroscopic redox activity. The results have significant potential to influence the design of water-splitting catalytic materials for tuning dimensionality, confinement, and charge delocalization across structures.

INTRODUCTION

Surface catalysis that utilizes inexpensive earth-abundant materials and easily scalable fabrication techniques is of vital importance to our global economy.[1-4] Recent fundamental research has identified transition metal oxides as robust sunlight absorbers, capable of efficiently converting light into useful forms of energy such as electricity or heat.[5-10] Amorphous cobalt oxides show great promise for undergoing artificial photosynthesis, mimicking the functionality of plants and microorganisms that split water into hydrogen and oxygen.[11-16] Both amorphous cobalt oxide films and cobalt oxo clusters are of fundamental interest and are widely investigated as models for the oxygen-evolving catalyst (OEC) in photosynthesis. These compounds act as earth-abundant electrocatalysts for water-splitting and bio-inspired light-harvesting systems.[17-26] Whereas previous artificial leaf devices have relied on relatively rare and expensive materials such as platinum, these amorphous cobalt oxides with oxyanions are cheap and can be easily grown through anodic electrochemical deposition with water-based buffer solutions in the presence of phosphate and borate for cobalt-phosphate (CoPi) and cobalt-borate (CoBi) respectively, while exhibiting remarkable OER performance.[24, 25, 27, 28] CoPi and CoBi both share a similar cobalt domain structure that makes them among the most robust electrocatalysts for water-splitting reactions.[27-31]

Currently, a major challenge is to elucidate the interplay between cobalt catalytic sites and bulk charge transport properties across the metal oxide surface to fully understand the CoPi material's electronic structure and potential for artificial leaf applications. To date, many studies have focused on the material's ground-state electronic properties and electrocatalytic function.[23, 25, 28, 32-34] Synchrotron-based X-ray absorption spectroscopy and scattering characterization on the CoPi material has been extensive owing to its robust physical and chemical properties.[23, 25, 27, 28, 32, 35] Previous studies have elucidated the electrochemical and ground-state electronic properties of amorphous cobalt oxides through *in situ*/*ex situ* extended X-ray absorption fine structure (EXAFS).[23, 32] Under electrochemical biasing, these studies suggest an oxidation state of greater than 3 for the onset of catalysis that is influenced by the molecular dimensions of the cobalt clusters. Additional Co L3 X-ray Absorption Spectroscopy (XAS) and Co Kβ Resonant Inelastic X-ray Spectroscopy (RIXS) concluded that the ground state consists of a mixture of two coordination geometries and spin states with 43.5% in a low-spin octahedral Co(III) and the remaining 56.5% in a high-spin octahedral or tetrahedral Co(II) state.[28, 36] *In situ* high-energy X-ray scattering and pair distribution analysis have been used to confirm domain size and the degree of sample crystallinity by looking at the length of oscillation coherence across large q space.[27] Conclusions from these studies indicate that catalysis occurs primarily at terminal oxo domain sites due to impeded inter-domain electron hopping and that the oxygen centers can facilitate orbital hybridization between

cobalt centers thus enabling charge delocalization and hole mobility in well-ordered thin films.[28]

Little is known about CoPi's excited-state photocatalytic properties and how the CoPi material interacts with visible light excitation. Recent studies suggest wavelength-dependent electrochemical photocurrent behavior indicative of photoanodic and photocathodic responses.[22] In this report, we investigate the early charge transport properties of the CoPi material and of related cobalt oxide complexes (CoBi) to understand the interplay between excited state photocatalytic properties and ultrafast carrier delocalization across the bulk material. X-ray Absorption Near-Edge Structure (XANES) is element-specific and contains redox and local structure information of the absorbing element, allowing for investigation of catalytic species as it relates to the domain size and inherent surface-to-bulk site ratio. Using this transient technique, we can observe the extent of charge renormalization and electron mobility at metal-metal or metal-ligand sites following intense pulsed photoexcitation. Pump-probe XANES is used to elucidate the oxidation state of the excited-state species that is correlated to optical transient absorption results where we track how the coordination geometry changes due to hole delocalization. We also employ optical transient absorption spectroscopy that identifies the presence of a long-lived electron 'trap' state persisting out to the microseconds timescale allowing for the discernment of restricted charge localization in the CoPi film compared with CoBi. Previous findings in Co L3 XAS and Co Kβ RIXS studies have demonstrated an intense off-diagonal emission peak at E_{tr}~ 61.5 eV for E_i = 7711.5 eV originating from nonlocal dipole transitions for Co-O-Co intersite hybridization between Co 4*p* and neighboring Co 3*d* orbital states with the presence of oxygen 2*p* in O_h Co(III) oxides.[28] Inherent material properties such as charge-transfer localization and electron mobility both under ambient and high temperature conditions are examined to determine the extent of thermal contributions to the photoexcited-state intermediate. These results will allow for the design of more effective cobalt-based OECs that require optimization of both individual cobalt catalytic centers and their electronic interactions with surrounding Co(II) or Co(III) metal centers and their oxo-ligands. By examining the impacts of bias potential, we can directly probe how shifting the Fermi level position[37] of CoPi/CoBi leads to changes in electron-hole recombination rates and surface charge transfers, and thereby develop a more nuanced picture of electronic information. We elucidate the nature of valence band hole localization and charge separation across metal-ligand bonds. The findings are generally applicable to the important fields of heterogeneous and interfacial catalysis, as well as the optimized design of functional metal oxides.

EXPERIMENTAL METHODS

Electrosynthesis of CoPi and CoBi. Electrosynthesis of thin films was carried out using a standard three-electrode electrochemical cell and a previously established procedure.[18, 22-25] For fabrication of the phosphate cobalt oxide (CoPi), a potassium phosphate (KPi) aqueous buffer electrolyte is combined with 0.5 mM cobalt(II) nitrate, then titrated to pH 7.0 using an aqueous solution of potassium hydroxide (KOH). Under bulk electrolysis bipotentiostat settings (CH Instruments, Inc.) the thin film electrodeposits at +1.34 V vs NHE onto the working electrode that consists of indium tin oxide (ITO) coated glass. A 2 mm pseudo-Ag/AgCl electrode was used as a reference, and the auxiliary electrode consisted of a 0.5 mm gauge platinum wire. For fabrication of the borate cobalt oxide (CoBi), a borate potassium aqueous buffer electrolyte is combined with 0.5 mM cobalt(II) nitrate, then titrated to pH 9.0 using an aqueous solution of potassium hydroxide (KOH). For bulk-electrolysis thin-film deposition settings, the same electrode configuration is used only with a set potential of +1.14 V for electrodeposition.

Nanoscale particle formation. Wet colloidal ball milling was undertaken to prepare the CoPi and CoBi samples for liquid jet X-ray transient absorption (XTA) spectroscopy measurements. Because prior high-energy X-ray measurements demonstrated a domain size of 13-14 atoms for CoPi and 40-50 atoms for CoBi,[27, 28] wet colloidal ball milling was utilized to create nanoscale particulates of the deposited material while still maintaining chemical and structural integrity.[38-40] Furthermore, dimethylformamide (DMF) was chosen as a suitable solvent due to its high flash point and ability to act as an efficient thermal dissipator when irradiated with intense high-energy X-rays and pulsed optical beams. Thin films were grown according to the above procedure followed by drying under an N_2 environment. Following film growth, redox cycling (+0.5 V to +1.55 V) of both the CoPi thin film in a KPi aqueous buffer and the CoBi thin film in a KBi aqueous buffer without the Co(II) precursor salt served to activate metal sites and remove the thin passivation layer. Without this step, the thin films do not exhibit robust photo-electrochemical behavior.[22] Following N_2 drying of the CoPi / ITO / glass electrode, the CoPi thin film was dispersed and dissolved into clusters (Figure S3) using DMF into an aluminum oxide (Al_2O_3) ceramic jar with 1 mm zirconia beads. The ceramic jar was then sealed with parafilm and clamped shut in a planetary ball mill that underwent 300 revolutions per minute for 2 hours total, with 30-minute segments at four changes of rotation directionality (PM 400 Retsch GmbH). Following wet colloidal milling, the liquid suspension was siphoned off using a glass Pasteur-pipette and stored temporarily in glass vials before characterization by the techniques listed below. The Al_2O_3 ceramic jar and zirconia beads were thoroughly rinsed and cleaned with DMF in between each use, then sonicated in a deionized water bath for 60 minutes and dried.

X-ray transient absorption measurements. Liquid jet solution phase measurements were carried out at the 11-ID-D beamline of the Advanced Photon Source[41, 42] using a high energy X-ray probe (Co K-edge 7.71 keV) in 24 bunch mode with a focused femtosecond optical pump (400 nm) which was the second harmonic generated output from a Coherent Ti:Sapphire regenerative amplifier system with an 800 nm fundamental operating at a 10 kHz repetition rate. The high flux monochromatic X-ray beam size was reduced from a typical beam size of 80 μm (v) x 550 μm (h) fwhm to a more focused beam size of about 100 μm (v) x 275 μm (h) to cover the entire jet on its horizontal position and to increase the overall excited state yield. Calculations indicate between a 0.94 to 8.7 percent excited-state fraction per laser pulse at 400 nm excitation (Supporting Information). Fluence studies were carried out on optical transient absorption setups prior to beamtime to determine the threshold fluence for two photon or multiphoton absorption effects at 400 nm excitation. Measurements at 11-ID-D were performed at these laser fluence values (1.6 nJ pulse^{-1} μm^{-2}) at 400 nm; additional laser pump fluence studies (80 nJ to 70 μJ) were performed at 11-ID-D to ensure this remained in the linear absorption regime. Time overlap between the X-ray probe and optical pump pulses were found using a 5 mM solution of

Ni(TMP) in toluene at the Ni K-edge (Figure S2). Following successful time overlap, the X-ray energy was tuned to the Co K-edge for all subsequent measurements. After wet colloidal milling, the CoPi and CoBi samples were loaded individually into a 20 mL cell held under constant N_2 atmosphere. A peristaltic pump (Masterflex L/S) with PTFE tubing was used to maintain a constant sample stream velocity in the X-ray probe/optical pump overlap region for good jet quality, and to refresh the sample between laser shots. Soller slits and Z-1 filters were prepared and refreshed after each sample batch where a total of five 20 mL sample batches were used at 60 mM concentration to increase the excited state fraction based on our calculations at a standard concentration of 20 mM. Two avalanche photodiode detectors (APDs) were mounted on either side of the liquid jet sample region at a 90 ° angle to the X-ray probe beam path laser optical pump. Step sizes for X-ray absorption near edge structure (XANES) experiments with both laser on and laser off sampling were drawn from previous experiments.[41-45]

***In situ* X-ray absorption spectroscopy under heating conditions.** A Linkam THMS 600 sample stage was used for heating measurements at 12-BM of the Advanced Photon Source.[46, 47] Both CoPi and CoBi thin films were grown according to the procedure described above, redox cycled, and dried under N_2 before being placed inside the X-ray sample chamber. Once inside the chamber, the thin films were purged with a N_2 mineral oil bubbler, and X-ray absorption studies were done under a N_2 atmosphere. Kapton tape was placed over the sample aperture to allow for fluorescence mode detection of X-ray absorption spectroscopy (XAS) studies at the Co K-edge (7.71 keV). A heating rate of 10 ℃/min was used with stability of < 0.1 ℃ over a range of 25 to 125 ℃. Data processing was performed in Athena 0.9.26 from the IFEFFIT package.[48]

Femtosecond transient absorption spectroscopy of *in situ* electrochemical dynamics. Optical transient absorption studies were performed using a 3D printed chemically resistant cell that is detailed in previous studies involving water-splitting CoPi thin films.[22, 49] Both front- and back-facing windows are made of 0.5 mm thick indium tin oxide (ITO) coated quartz glass (10-20 ohms, Delta Technologies, LTD) machined to size. The front-facing quartz glass window became the working electrode by connecting thin conductive copper tape to the surface with a layer of clear epoxy to coat the point of contact only. CoPi and CoBi thin films were grown *ex situ* on front-facing windows and epoxied with the film side facing inward. A phosphate aqueous electrolyte and a borate aqueous electrolyte were used for the CoPi and CoBi *in situ* studies, respectively. A PTFE Teflon lid was machined to hold the 2 mm *pseudo* Ag/AgCl wire reference electrode,[22] the 0.5 mm platinum wire auxiliary electrode, a 1/16" outer diameter PTFE Teflon tubing for a constant N_2 purge, and another 1/16" opening functioning as a gas outlet. A valve connected to a syringe pump was incorporated to reduce O_2 bubble accumulation at the thin film surface. The electrochemical cell was fastened to a 2D raster scan stage (Zaber Technologies, X-NA08A25) where the sample was translated vertically and horizontally in between each scan to sample new areas on the thin film electrode. The output of a Spectra-Physics MaiTai Ti:Sapphire oscillator was used to seed a Spitfire regenerative amplifier cavity pumped by a high-energy Q-switched Empower laser. The output of the regenerative amplifier consists of an 830 nm fundamental with a 100-fs pulse duration at a 1 kHz repetition rate and 2.75 W of average power.[44, 50-53] About one quarter of the fundamental was used for second harmonic generation (415 nm) in an LBO-I crystal, white light continuum generation to seed optical parametric amplification, and generation of the white light continuum probe inside the spectrometer. The portion of the fundamental that is reflected off a thin film polarizer is used to generate white light in a sapphire crystal that then seeds a two-stage home-built optical parametric amplifier[54] tuned to 600 nm. Both the OPA signal (600 nm) and the portion of the SHG signal (415 nm) unused for parametric amplification were sent into a transient absorption spectrometer (Helios, Ultrafast Systems). The portion of the fundamental that transmitted through the thin film polarizer was also directed into the spectrometer for white light continuum generation in a sapphire crystal (3 mm thick). An optical chopper operating at half the repetition rate (500 Hz) allows for shot-to-shot pump-on and pump-off acquisition of the transient absorption signal detected using a complementary metal-oxide semiconductor (CMOS) line scan detector interfaced with data acquisition software (Ultrafast Systems). The pulse duration of the fundamental was measured as 135 fs at the sample stage using a single-shot autocorrelator (Delta Single Shot, Minioptic Technology Inc.) and oscilloscope (Tektronix Inc). The width of instrument response function (IRF) for both ambient thin films and aqueous electrolyte cell conditions was determined to be 243 fs for the 600 nm optical pump and 545 fs for the 415 nm optical pump.

UV-Vis spectrophotometry and spectro-electrochemical characterization. The absorption spectra of the CoPi and CoBi thin films were collected using a Beckman-Coulter DU800 Spectrophotometer in transmission mode, baselined to thin ITO glass. Spectro-electrochemical characterization was carried out using a 2 mm quartz cuvette with a machined PTFE Teflon top to hold the thin film working electrode, *pseudo* Ag/AgCl wire reference electrode,[22] and platinum auxiliary electrode in place following purging with N_2. Bulk electrolysis mode in a CH Instruments 700E bipotentiostat was used and the oxidation state of the thin films were allowed to equilibrate for at least 30 minutes before spectra were taken. For colloidal samples, absorption spectra were taken immediately after wet solution phase processing in DMF.

Nanosecond transient absorption spectroscopy. Using a previously reported setup (Figure S4),[50, 53, 55] the transient signal response was recorded using a 1 kHz Ekspla PL2210 Nd:YAG diode-pumped mode-locked laser with a fwhm pulse duration of 25 ps where the third harmonic output was used to pump an Ekspla PG403 optical parametric generator (OPG) with output range of 410-1000 nm to form the pump excitation pulse for transient absorption measurements at a 0.5 kHz repetition rate using the pulse picker modality to allow for successive pump on/pump off spectra. The probe pulse was formed using the output of a ~1 m length photonic crystal fiber coupled to a 1 kHz Leukos STM-1-UV supercontinuum 600 picosecond fwhm pulsed source. The master clock from the Ekspla Nd:YAG laser was used to synchronize the probe (Leukos) with the pump (OPG) to find time zero overlap electronically using transistor-transistor logic (TTL) additive and subtractive combinations, and to delay the probe relative to the pump on nanosecond timescales with a temporal measurement window of -10 ns to 950 μs. A probe spot size of ~100 μm in diameter was achieved at the sample where the signal was collected in the same direction as the probe and focused using a f-matched 150 mm focal length lens into a SP-2150i Acton Series spectrograph with a turret grating set to 150 g/mm blazed at 800 nm dispersing the signal onto a Teledyne DALSA Spyder3 SG-14 CCD camera. Data

was collected using LabVIEW 2014 software with an instrument response time of ~1 ns. The pump was tuned to 415 nm with pulse energies ranging between 350 nJ to 13 μJ per pulse, and a probing window of 400 to 800 nm.

Near-ultraviolet region femtosecond transient absorption spectroscopy. A mode-locked Ti:sapphire laser and regenerative amplifier (Astrella, Coherent Inc.) was used to probe near-ultraviolet spectral dynamics in thin films on the femtosecond timescale. The system consists of a 1 kHz repetition rate laser with an 800 nm fundamental beam and temporal width of 100 fs full-width-half-max.[56, 57] A portion of the output was sent to generate the pump beam through optical parametric amplification (OPerA Solo, Coherent Inc.) tuned to 400 nm at 800 nJ/pulse with the remainder focused onto a 4 mm CaF_2 crystal to generate a broadband continuum in the 350-750 nm wavelength range. The polarization between pump and probe beams was set to the magic angle of 54.7° with data acquired using a CCD spectrometer (Ocean Optics, Flame-S-UV-vis-ES) and LabVIEW (National Instruments) software with continuous N_2 flowed over the thin film surface.

Oxygen evolving measurements with photo-electrochemistry. *In situ* studies of the catalytic behavior of CoPi and CoBi thin films were performed according to a previously described procedure and setup.[22] Briefly, a Clark-type nanosensor (Unisense OPTO-3000) was used with a MicroOptode Uniamp single-channel detector for sensing dissolved O_2 in liquid electrolytes. The sensor system was calibrated to 100% saturation by purging the liquid electrolyte cell vigorously with compressed air and calibrated to 0% saturation using a zero-oxygen calibrant solution (Unisense). Corresponding electrochemical measurements were performed using a three-electrode bipotentiostat system described above (CH instruments, Inc).

Scanning electron microscopy. Thin film surfaces and drop casted colloidal samples were imaged using a JSM-6010LA JEOL analytical scanning electron microscope at a beam voltage of 20 kV. Prior to imaging, samples were sputter coated with a 5-angstrom layer of gold for enhanced conductivity using a vacuum thin film deposition chamber (Denton Desk V).

RESULTS AND DISCUSSION

Dimensionality and Structural Ordering of CoPi and CoBi: Following the electrosynthesis of the compounds in Figure 1 as previously described above, the thin films and nanoscale colloidal suspensions were characterized by UV-Vis spectrophotometry. Scanning electron microscopy (SEM) images of both types of samples can be found in Figure S3. The CoPi thin film surface is shown in Figure S3a with domains consisting of 13-14 cobalt atoms as determined by high-energy x-ray scattering and computational simulations.[27, 28, 31] Following solution processing and drop casting onto silicon wafers coated with a 5-angstrom layer of gold for imaging, the SEM micrographs depict a typical structure with size less than one micron for CoPi (Figure S3b) and CoBi (Figure S3c) that were flowed through the liquid jet assembly following additional syringe filtration. The ground-state absorption spectra were normalized to the highest intensity feature. As shown in Figures 1c and 1d, the optical absorption of CoPi and CoBi respectively show distinct spectral peaks and features in the ultraviolet to visible region that are dissimilar from the known absorbance properties of cobalt oxides films (e.g. Co_3O_4, cobalt oxyhydroxides, etc).[11, 58-61] Due to their long-range crystal structure and periodicity, traditional cobalt oxides exhibit featureless and unremarkable optical properties in the ultraviolet-to-visible light region.[25, 27, 28] Consequently, the observation of these discrete electronic transitions in the CoPi and CoBi optical spectra is a striking departure from the more conventional compounds like Co_3O_4 and amorphous cobalt catalysts generally.[58, 59] In Figure 1c, the optical spectrum of CoPi displays peaks near 290 nm, 400 nm, and 670 nm.

The features have been previously assigned as photo-reductive (400 nm) and photo-oxidative (670 nm) transitions according to wavelength-dependent studies performed under *in situ* electrochemical conditions also known as photoelectrochemistry.[22] Similarly, the optical spectrum of CoBi (Figure 1d) shows low-intensity peaks at 300 nm and 400 nm with broadened features in the near-infrared region from 600-700 nm. Furthermore, a change in dimensionality is observed in going from the thin film optical properties of CoPi to those of CoBi, as evidenced by the gradual loss in sharpness of discrete electronic transitions in favor of vibrationally broadened and less intense spectral features. A comparison within the same compound shows that peaks observed in the optical spectrum of thin films are essentially retained in the nanoscale colloidal suspensions. As shown in Figure 1c, the same transitions near 290 nm, 400 nm, and 670 nm also appear in the CoPi colloidal suspensions in DMF as they do in the CoPi thin films. Likewise Figure 1d shows similar transitions near 300 nm and 400 nm for both the CoBi colloidal suspensions in DMF and in the CoBi thin films. These similarities allow for the direct comparison between X-ray transient absorption measurements (XTA) of colloidal suspensions with those of thin-film sample configurations under *in situ* heating and electrochemical conditions using optical pump-probe spectroscopy.

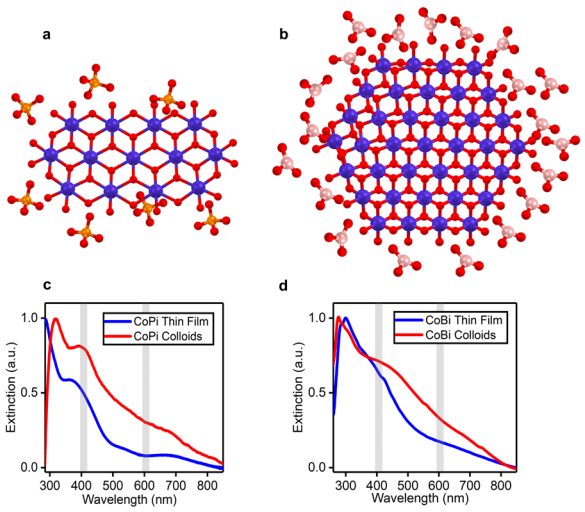

FIG 1. (a) CoPi domain size with phosphate anions (b) CoBi domain size with borate anions (c) ground state absorption characteristics of the CoPi thin film (blue) and the CoPi colloids (red) in dimethylformamide (d) ground state absorption characteristics of the CoBi thin film (blue) and the CoBi colloids (red) in dimethylformamide. Elements are color-coded as follows: cobalt (blue), oxygen (red), phosphorous (orange), boron (pink). The vertical grey lines represent optical pump excitation wavelengths.

Net Photoreduction and Enhanced Reversibility with Greater Interlayer Electron Delocalization: Colloidal suspensions in DMF were studied by x-ray transient absorption spectroscopy in a liquid jet assembly under 400 nm pulsed

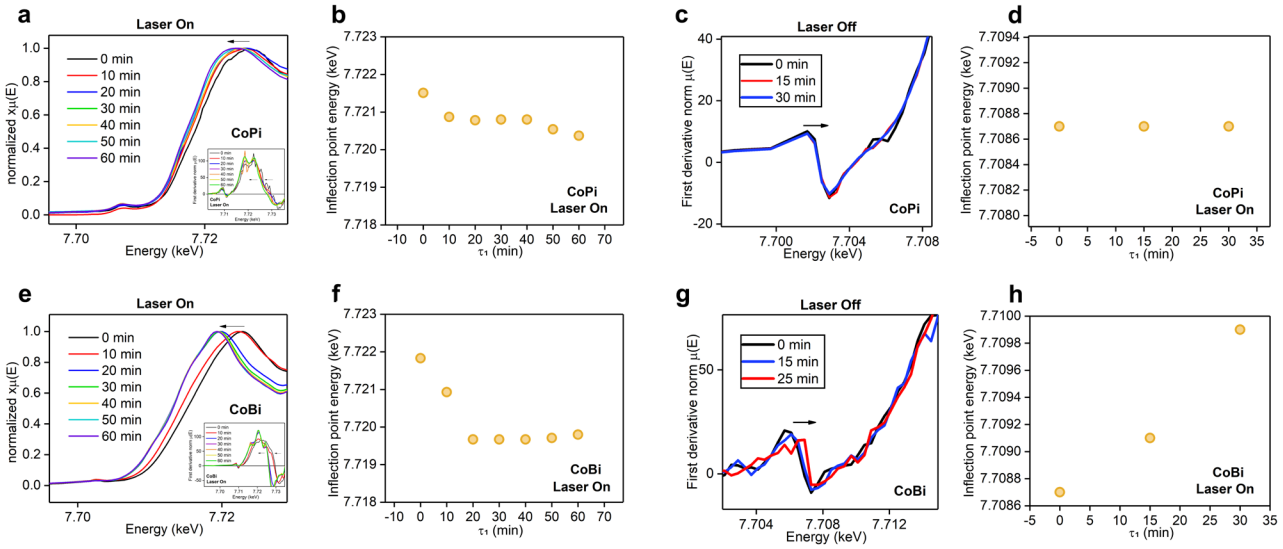

FIG 2. Co K-edge XANES as a function of 400 nm pulsed irradiation time for (a) CoPi and for (e) CoBi. Time dependent drift of the peak of the first derivative of the Co K-edge feature for CoPi with laser on for (b) CoPi and for (f) CoBi. Subsequent laser off scans of the ground state for (c) CoPi and for (g) CoBi. Time dependent drift of the first derivative of pre-edge features for (d) CoPi and for (h) CoBi. Ground state XANES measurements with laser on and laser off illumination were performed in the same configuration as excited state XANES measurements.

optical illumination in an N_2 atmosphere. A pump power dependence study was performed on CoPi thin films at fluences ranging from 350 nJ to 13 μJ with a beam waist spot size of ~250 μm (Figure S5). Spectra in Figure S5a indicate the linear absorption regime. Pump power was sequentially increased until sudden multi-photon absorption effects were observed that include differences in relative peak intensities in the 400 – 580 nm region along with a large featureless background between 600 – 800 nm (Figure S5b) establishing the threshold fluence of about 1 nJ pulse^{-1} μm^{-2} for the initial onset of pronounced differences in nonlinear spectral features through time. At fluences within the linear absorption regime (Figure S5c and S5d), the excited-state population is seen to fully relax back to the ground state by 100 μs, but with the majority of signal decayed within 10 μs, which ensures the 10 kHz repetition rate laser used in the XTA beamline measurements will not re-excite the sample. A fluence of 1.6 nJ pulse^{-1} μm^{-2} at 400 nm was chosen for all XTA measurements shown below to maximize transient difference signal counts at the beamline while also remaining in a comparable flux regime to our optical nano- and femtosecond TA measurements. Both CoPi and CoBi colloidal suspensions were first characterized at the Co K-edge (7.71 keV) in the X-ray absorption near edge structure (XANES) region and compared to steady-state measurements of the thin film surface. Figure S6a and S6b show agreement in the XANES spectra of CoPi and CoBi in both colloidal and thin film sample forms. A slight edge shift (< 1 eV) is observed between the films and colloidal suspensions where the source of that shift is either due to fragmentation of the counter anions (potassium phosphate and borate phosphate groups) and reassembly with the metal-oxo colloidal domains. Following ground-state XANES characterization at the Co K-edge, the colloidal suspensions were photoexcited with 400 nm and the ground-state XANES spectra ('pump off') were monitored in between each photoexcited scan ('pump on'). Figures 2a and 2e show a shift to lower energies of the edge feature for both the CoPi and CoBi compounds following prolonged irradiation. The same can be seen in the inflection point of the normalized first derivative μ(E) when comparing between photo-induced behavior of CoPi and CoBi (Figure 2a (inset) and 2e (inset), Figure S7). Additionally, the pre-edge in CoPi is observed to be stronger than CoBi due to smaller domains and more unsaturated bonds at domain edges which give enhanced 3*d*-4*p* mixing. The rate of change in the edge feature is quantified in Figures 2b and 2f which can be correlated to the dimensionality of the material.[27, 28, 31] Previous resonant inelastic X-ray scattering (RIXS) measurements have demonstrated electron hopping between Co-O-Co bridged sites in CoBi, an effect that contributes to this compound's very robust water-splitting properties under electrochemical conditions. This effect was attributed to rapid intralayer electron delocalization in the excited state followed by slow interlayer hopping electron transfer.[28] Because of its smaller domain size, CoPi in contrast exhibited impeded inter-domain electron hopping and thus less charge delocalization in general. CoPi, with its smaller dimensionality and less charge delocalization, is slower to change its electronic behavior when experiencing prolonged irradiation with 400 nm. In contrast, CoBi is faster to edge shift its XANES spectra due to its larger dimensionality and more charge delocalization. Comparing Fig. 2b (CoPi) to Fig. 2f (CoBi), a pronounced energy shift of 3 eV is observed within the first 20 minutes of photo-illumination for CoBi whereas under identical conditions CoPi exhibits less than a 1 eV shift to higher energy. Similarly, a difference in dimensionality is also noticed in the recovery time of the XANES edge shift. For CoPi, the edge is not observed to shift back towards higher energies after shuttering of the 400 nm optical laser (Figure 2c and 2d). In contrast, the CoBi material is observed to shift back towards higher energies with a pre-edge absorption broadening (Figure 2g and 2h) at a rate and at a value greater than that of CoPi under the same conditions. For CoBi, an energy shift of -3 eV is observed (Fig. 2h) whereas CoPi exhibits no energy shift or recovery following photo-illumination (Fig. 2d). Our observations demonstrate that CoPi displays a smaller total shift (< 1 eV) when compared to CoBi (3 eV) when photoilluminated. Afterwards, CoPi has little to no recovery whereas CoBi does exhibit strong recovery after photoillumination when the light is off. Differences in domain size provide an explanation for this perceived difference with the average CoBi cluster being 3-4 nm in size with coherent interlayer

stacking structure, compared to the smaller and unstacked structure of CoPi.[28, 62] Furthermore, the potassium phosphate counter anion structure is electron donating whereas the potassium borate counter anion structure is electron withdrawing, leading to further enhancement of charge back-transfer within layered sheets and greater electron mobility when photo-excited at 400 nm (Fig. 2e).[63]

Previous studies on first row transition metal oxides as thin films, such as iron oxides (Fe_2O_3) and copper oxides (CuO), show that certain XTA signals can be explained by photoinduced lattice thermal effects.[44, 64] Therefore, *in situ* heating measurements of the CoPi and CoBi thin films were carried out for comparison with the XTA signal of CoPi and CoBi colloidal suspensions in a thermally dissipative solvent (DMF). Figure S8 shows the macroscopic effects of large temperature gradients across the CoPi and CoBi thin film surfaces under N_2 atmosphere with pronounced changes in the peak intensity at the white line and in the fine-structure region. As the CoPi thin film is heated from 25 °C to upwards of 225 °C, a change is observed in both the steady-state X-ray absorption near edge structure (XANES) and the extended X-ray absorption fine edge structure (EXAFS) regions (Figure S9).

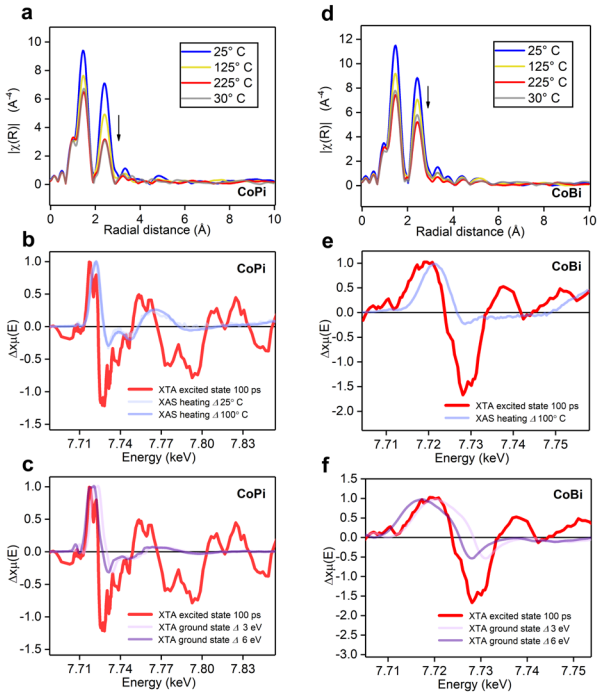

FIG 3. *In situ* heating EXAFS of (a) CoPi thin film followed by the transient X-ray probe and optical pump difference signal at 100 ps compared to (b) XAS heating difference signals and (c) simulated reductive difference signals. *In situ* heating EXAFS of (d) CoBi thin film followed by the transient X-ray probe and optical pump difference signal at 100 ps compared to (e) XAS heating difference signals and (f) simulated reductive difference signals. Heating begins at 25 °C to 125 °C to 225 °C then back down to 30 °C. XAS difference spectra were generated from data in Fig. S8 (Δ25 °C and Δ100 °C).

The Fourier-transformed (FT) EXAFS spectra show a clear decrease in peak intensity with increasing macroscopic temperature gradients across the thin film surface. As the temperature is cycled and the thin film is cooled back down to room temperature, the EXAFS spectra do not recover completely in peak intensity for both the CoPi and CoBi compounds (Figure 3a and 3d), with CoBi showing a slight intensity increase in peak intensity following cooling to 30 °C compared with the last heating spectra at a high-temperature point of 225 °C. The same effect was not observed in CoPi. A FEFF analysis for CoPi shows that sites are nominally octahedral geometry prior to heating, and that after heating there is a decrease in the SO2 amplitude due to a degree of disorder within the system (Figure S9, Table S1). Furthermore, a comparison of the XTA difference signal (pump on / pump off) with the heating XAS spectra shows that the photoexcited response cannot be completely explained by lattice thermal dissipation alone (Figure 3b and 3e). Here the transient signal at 100 ps time delay between the X-ray probe and optical pump shows different features than those in *in situ* heating XAS measurements for temperature changes of 25 °C and 100 °C. Similarly, the photoexcited state at 100 ps was compared to a 3 eV and 6 eV reductive shift in the ground state XANES spectra for both CoPi (Fig. 3c) and CoBi (Fig. 3f). A shift of magnitude 3 eV correlates to an oxidation state shift (e.g. Co(II) to Co(III)) as determined by redox titration XANES measurements at the Mn, Co, and Ni K-edges.[36, 65] Lower energy features in both CoPi and CoBi can be interpreted as resulting from a combination of thermal and reductive processes. For example, the XTA dual peak feature in the CoPi first-derivative spectra centered at 7.72 keV could be composed of contributions from thermal effects at energies of 7.76 keV or greater (Fig. 3b and 3e) and lower energy contributions from charge-transfer-coupled redox activity (Fig. 3c and 3f). The first derivative of the ground state XANES also displays a dual-peak feature, which corresponds to two edge absorption bands. Thus, the dual feature in the XTA results from the red-shifting of these two edge absorption bands. Likewise, the 7.717 keV feature in CoBi can have contributions from both heating and photoreduction where we infer that absorption features in the XANES spectra relae to the local structure and electronic transitions in the metal through a combination of photothermal and photochemical deactivation pathways. Whereas the observed photoexcited XTA spectra were mildly reversible, especially in CoBi samples, the heating XAS spectra were mostly irreversible. Such results are suggestive of a chemically-driven process over a purely photophysical process and that the slow long-term process is, at most, mildly photodriven. An implication of the findings suggests that the photoexcited changes are due to a mixture of electronic and thermal pathways, with the later being irreversible.

Fast Decay Rates with Increase in Trap States: Femtosecond time-resolved optical kinetic studies were carried out under *in situ* electrochemical conditions for the identification of the photoexcited species at 415 nm from a time delay of -10 ps to 3 ns. These measurements are shown in Fig. 4 and Fig. 5 for CoPi and CoBi with extended time delay ranges and kinetic analysis in Fig. S14 through Fig. S22, Tables S2 – S6. A detailed schematic of the 3D printed electrochemical cell for femtosecond transient absorption spectroscopy can be found in Figure S10 along with a schematic of the optical transient absorption setup for femtosecond timescale studies. Additional studies were also performed using a 600 nm pump for wavelength-dependent comparison of the decay dynamics. The beam size dimensions were comparable between experiments with the 415 nm spot having a diameter of 252-257 μm and the 600 nm spot having an elliptical shape with axes of 224 μm and 115 μm (Figure S11). The white light continuum probe was approximately 111 μm in diameter ensuring all species probed were in the electronically excited-state since the pump spots are comparatively larger in diameter. Prior to *in situ* electrochemical transient absorption measurements, the CoPi thin films were redox cycled

and their cyclic voltammograms were recorded (Figure S12) which were consistent with previous findings for a heterogenous ground state of Co(II)/Co(III) with high valency states of Co(IV) present at increasingly oxidative potentials.[22, 66] Figures 4a and 4b show the femtosecond transient absorption spectra for the CoPi and CoBi thin films biased at +0.9 V—still in the electrochemical ground state—while photoexcited by a 415 nm optical pump. Initially at 500 fs, stimulated Raman features, dip near 480 nm, are observed due to the presence of aqueous electrolyte and cross-phase modulation between the pump-probe beams followed by the appearance of a peak at 500 nm in CoPi. At 1 ps, the peak then shifts to higher energies centered at about 480 nm with the appearance of a secondary feature at 580 nm and a low-intensity, broadened feature centered about the near infrared. Between 1 ps and 50 ps, the spectra evolve such that the background diminishes, and the electronic features stabilize with a peak at 480 nm and a secondary peak at 700 nm. This spectral profile equilibrates and persists out to the microsecond timescale regime as seen in the nanosecond transient absorption measurements (Fig. S5). Figure 4b shows the electrochemical transient absorption spectra of CoBi biased at +0.9 V. A similar time evolution is observed for CoBi with increased intensity in the 575 nm to 725 nm region. Like CoPi, the CoBi transient absorption spectrum displays a prominent peak at 500 nm at early time delays (< 1 ps) with localization that occurs on timescales of 50 ps or greater. For CoBi, a prominent secondary peak is observed at 10 ps centered at 700 nm. According to prior studies on cobalt phosphate catalysts such as pakhomovskyite (Co3(PO4)2·8 H2O, Pak) and the phosphate-containing Co oxide (CoCat), we assign visible and ultraviolet transient absorption frequency-resolved features centered at 313 nm and 700 nm to Co(II) following the UV-Vis absorption spectral features of the thin film prior to redox poising.[67] Features centered at 350 nm, 520 nm, and 790 nm can be attributed to Co(III) according to the spectro-electrochemical absorption peaks that grow in from an applied bias of 1.35 V (vs NHE)[67]. Higher oxidation states can be assigned using spectro-electrochemical studies on the Co_4O_4 molecular structure regarded as an electronically active subunit of CoPi/CoBi that contains Co(IV) features centered at 550 nm.[35]

Considering these assignments, we can observe the following trends in our spectral data with 415 nm excitation. Whereas the time-resolved XANES measurements distinctly show a LMCT electronic transition (Fig. 2 and Fig. 3), the optical femtosecond TA can detect both ligand-to-metal charge transfer (LMCT) in Co^{2+} sites and metal-to-metal charge transfer (MMCT) transitions in adjacent Co^{3+} sites predicted by Co L3 XAS and Co Kβ RIXS studies.[27, 28] In the optical transient absorption data, we observe spectral signatures for the Co(IV) species that is formed pre- 500 fs given the absorption peak at 550 nm. This Co(IV) spectral peak localizes at 1 ps as seen by the appearance of a well-defined absorptive peak centered between 550 to 580 nm and later equilibrates on timescales of 10 ps or longer due to vibrational cooling. From 500 fs to 10 ps, the 550 nm Co(IV) species decays while the 520 nm Co(III) and the > 750 nm Co(III) features persist past 10 ps and decay together on longer timescales. The Co(III) feature localizes on the 1 ps timescale with a prominent peak at 520 nm and greater than 750 nm. We can infer that the photo reductive transition, or ligand-to-metal charge transfer (LMCT), and the metal-to-metal charge transfer (MMCT) take place on timescales < 500 fs because of increased Co(IV) signatures at early timescales that then dissipate after 10 ps yielding Co(III) and Co(II) spectral absorption peaks. Additionally, using a calcium fluoride (CaF_2) crystal for white light continuum generation, a spectral

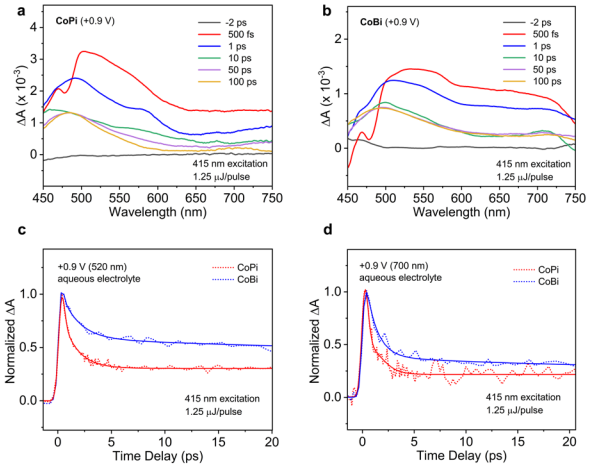

Figure 4. *In situ* electrochemical optical transient absorption of (a) CoPi and (b) CoBi in the electrochemical ground state (potential = +0.9 V). Kinetic traces probed at (c) 520 nm and (d) 700 nm for both CoPi and CoBi electrodes photoexcited with a 415 nm optical pulse. Experimental data is shown overlayed with a fitting function that incorporates a multiexponential decay convoluted with a gaussian instrumental response.

signature for Co(III) was observed at 350 nm (Figure S13) on early timescales of 500 fs consistent with our assignments above. When comparing electrochemical transient absorption spectra between the CoPi and CoBi electrodes, we notice an increased absorptive signal in the 600 nm to 725 nm spectral region corresponding to a greater population of photo-generated Co(II) species in CoBi due to a combined LMCT/MMCT transition with enhanced inter-domain electronic motion that prolongs the lifetimes of the LMCT/MMCT excited states.[22] Likewise, the CoBi electrode displays increased vibrational cooling of the electronic resonances at timescales of > 10 ps due to enhanced charge transfer between layers. This is due to the longer range ordering of CoBi thus being more structurally coherent and similar to a CoO(OH) layered structure with 3-4 nm cluster coherent domains in contrast to CoPi that consists of much smaller domain clusters with no coherent stacking or interlayer effects.[27, 28, 62, 63] Figure 4c shows kinetic decay traces probed at 520 nm for both the CoPi and CoBi electrodes and probed at 700 nm (Fig. 4d) in aqueous electrolyte at a redox potential of +0.9 V. The CoBi electrode shows a slower rate of decay on the < 5 ps timescale compared to the CoPi electrode. Additionally, the normalized CoBi electrode shows a greater excited-state fraction of trapped charge carriers when compared to CoPi, as seen by the increased amplitude of the decay kinetic shelf feature. This difference is more pronounced when probed at bluer wavelengths (520 nm) or at higher energies (Fig. 4c), than at redder wavelengths (700 nm) or at lower energies (Fig. 4d).

When observing the decay kinetics across varying electrochemical potentials, we notice that the excited-state fraction of trapped charge carriers increases with increasing set potentials. As seen in Figure 5 the long-lived trapped charge carriers are redox potential dependent. An increase in oxidative potential causes a pronounced increase in the ΔA signal of the CoPi electrode when pumped with 415 nm. The extent of this kinetic

shelf increases with applied potential and the trapped charge carriers persist out to the tens of microseconds timescale (Fig. S5). This effect is not seen with 600 nm excitation (Fig. 5b).

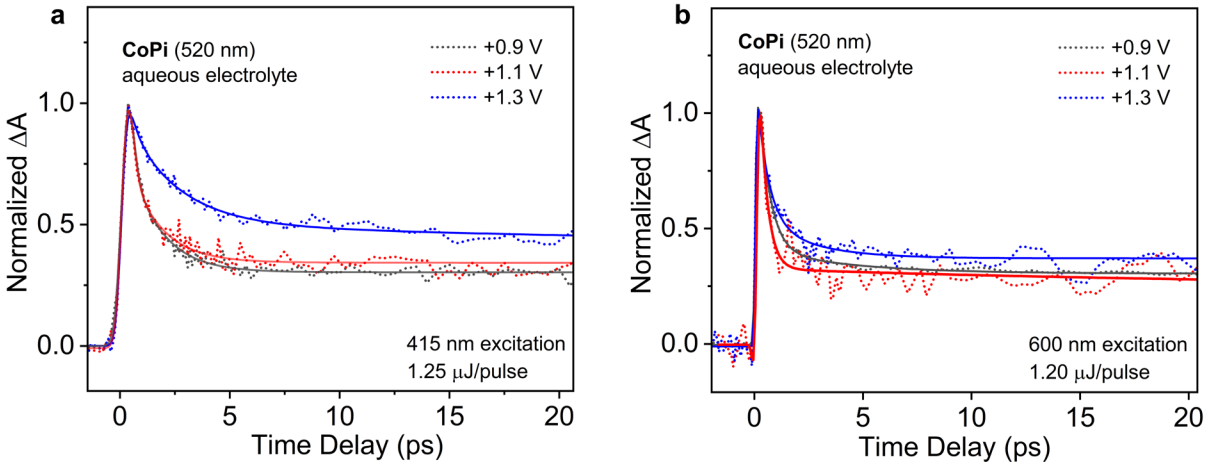

Figure 5. *In situ* electrochemical optical transient absorption of the CoPi electrode in aqueous electrolyte pH 7.0 probed at 520 nm under (a) 415 nm excitation and (b) 600 nm excitation. Redox potentials are swept from low oxidation states +0.9 V to high oxidation states +1.3 V.

The potential dependence under 415 nm illumination can be interpreted within the context of our previous photoelectrochemistry measurements[22] where blue light excitation is associated with an LMCT resonance from (hydr)oxo-Co(III) centers in the domain that when located at edge sites act to formally cause a reduction of the Co(III) to Co(II) while creating a larger population of trap states within the optical gap.[63] Kinetic analysis at three wavelengths (520 nm, 625 nm, and 700 nm) shows differing decay dynamics with the presence of several lifetimes (Figure S15, Table S2). A multiexponential decay function convolved with a Gaussian instrument response was used in fitting the first-order kinetics of the transient spectra, similar to previous studies.[46, 52, 53, 57, 68, 69] Following transient absorption studies both in ambient conditions (air) and in an electrolyte cell with redox biasing at voltages corresponding to cobalt oxidation state set points, the data was analyzed and the time constants were interpreted within the context of existing metal oxide literature compared with the excited state lifetimes in hematite (α-Fe_2O_3).[34, 44, 70-74] At 520 nm, the CoPi electrode under 415 nm illumination is seen to exhibit four decay lifetimes[44] in air corresponding to hot carrier formation (503.2 fs ± 174.6 fs, < IRF) followed by carrier thermalization via lattice dissipation or the relaxation of hot carriers (1.539 ps ± 0.5023 ps). Free carrier absorption and fast recombination then occurs (10.68 ps ± 5.665 ps) with incomplete lattice cooling (1.307 ns ± 305.1 ps) and the persistence of a long-lived charge trapped state past the detection window of the instrument. When the set potential of the CoPi electrode is at +0.9 V in an aqueous electrolyte, the intermediate lifetime that corresponds to fast recombination is quenched. Instead, a fast lifetime for hot carrier formation is observed within the instrument response function limit (τ_1 < IRF) followed by standard lattice dissipation (1.432 ps ± 0.1138 ps). The long lifetime or τ_4 is also observed to increase. A normalized plot of the kinetic decay traces shows the highest concentration of trapped charge carriers localized near 520 nm which is especially apparent at a high oxidation potential of +1.3 V (Fig. S15d) with Co(III) and Co(IV) sites.

A kinetic analysis was also performed on the CoBi electrode under 415 nm illumination (Fig. S16, Fig. S17, and Table S3). Similar lifetime assignments to CoPi can be made for CoBi in air when probed at 520 nm such as hot carrier formation that is within the instrument response function limit, carrier thermalization (2.319 ps), free carrier recombination (52.33 ps) and incomplete lattice cooling with the formation of a long-lived charge carrier trap state (903.7 ps). In CoBi, the hot carrier lifetime, the carrier thermalization lifetime, and the recombination lifetime are all seen to decrease with increasing oxidation potential while the long-lived lifetime corresponding to incomplete lattice cooling and charge carrier trapping is seen to increase. As seen with CoPi, the CoBi electrode shows a greater population of long-lived trapped charge carriers when probed at 520 nm compared to probing at 625 nm or 700 nm (Fig. S17, Fig. S20). This difference is quantitatively most pronounced at high oxidation potentials, such as +1.3 V (Fig. S17d). When the CoPi electrode is excited using a 600 nm pump, a Co(IV) feature is unobserved (Fig. S18) unlike the CoPi spectrum with 415 nm pump at 1 ps time delay (Fig. 4a). A kinetic analysis probed at 520 nm for CoPi with 600 nm pump shows lifetimes that can also be assigned to hot carrier formation, carrier thermalization, and recombination (Table S4) with an absence of the long-lived species. Using a 415 nm optical pump, a power titration was performed at a voltage bias of +1.3 V to observe the impact of increased photon absorption on kinetic decay rates. For CoPi, all fast lifetimes were observed to increase with increasing fluence (Fig. S21, Table S5) with a greater portion of the transient absorption signal being dominated by early processes such as hot carrier formation that is within the IRF of the measurement, rather than vibrational cooling picosecond timecales. Differing dynamics were observed for CoBi where a decrease was observed in the relative contributions of hot carrier formation to the overall signal with increasing pump fluence (Table S6). For CoBi, the transient absorption decay kinetics has a greater contribution from later processes (τ_2, τ_3) such as lattice dissipation dynamics and recombination likely due to the interlayer stacking structure of the electrode material and increase in dimensionality that is also linked to the increased lifetime (Fig. 4c) as a potential precursor state to water-splitting catalysis.[73, 75] A higher fraction of trap states was observed for CoBi than CoPi implying dimensionality, charge delocalization, and the relative proportion of surface states plays a role in water-splitting reactions.

Implications for oxygen-evolving reactions: We investigate electronic and thermal changes in CoPi and CoBi oxygen-

evolving catalysts to better understand how structural components such as domain size and interlayer coherence play a role in charge transport and trapped states within the material

potential swept from +0.71 V to +1.51 V. For both the CoPi and CoBi anodic electrode, a rise in the O_2 concentration starts to increase during the backward (reductive) scan as indicated by

Table 1. CoPi *in situ* electrochemical transient absorption decay lifetimes.

Metal oxidation state CoPi anode	Spectral absorption (wavelength, nm)	Ambient conditions (air, open circuit voltage)	Electrolyte conditions (aqueous buffer, +1.3 V)
Co(II)	313, 700[1]	τ_1: < IRF τ_2: 1.364 ps ± 0.240 ps τ_3: -- τ_4: --	τ_1: < IRF τ_2: 1.298 ps ± 0.123 ps τ_3: 15.66 ps ± 2.989 ps τ_4: 828.7 ps ± 142.9 ps
Co(III)	350, 520, 790[1]	τ_1: < IRF τ_2: 1.539 ps ± 0.50 ps τ_3: 10.68 ps ± 5.66 ps τ_4: 1.307 ns ± 305. ps	τ_1: < IRF τ_2: 2.353 ps ± 0.315 ps τ_3: 49.89 ps ± 11.10 ps τ_4: 1.113 ns ± 172.7 ps
Co(IV)	550[2] (fitted 625)	τ_1: < IRF τ_2: 4.346 ps ± 1.767 ps τ_3: -- τ_4: --	τ_1: < IRF τ_2: 1.931 ps ± 0.184 ps τ_3: 37.92 ps ± 8.847 ps τ_4: 2.471 ns ± 1.426 ns

[1] Reference 57. [2] Reference 35. Fitted decay lifetimes correspond to hot carrier formation (τ_1), carrier thermalization via lattice dissipation (τ_2), free carrier absorption and fast recombination (τ_3), lattice cooling and long-lived charge trap states (τ_4), References 34, 42, 64-68. τ_1 is within the IRF of the measurement.

Table 2. CoBi *in situ* electrochemical transient absorption decay lifetimes.

Metal oxidation state CoBi anode	Spectral absorption (wavelength, nm)	Ambient conditions (air, open circuit voltage)	Electrolyte conditions (aqueous buffer, +1.3 V)
Co(II)	313, 700[1]	τ_1: 687.7 fs ± 312.0 fs τ_2: -- τ_3: 16.14 ps ± 15.39 ps τ_4: 917.1 ps ± 1150 ps	τ_1: 545.1 fs ± 194.5 fs τ_2: 2.304 ps ± 0.694 ps τ_3: 19.64 ps ± 5.984 ps τ_4: 590.2 ps ± 98.61 ps
Co(III)	350, 520, 790[1]	τ_1: < IRF τ_2: 2.319 ps ± 0.547 ps τ_3: 52.33 ps ± 19.70 ps τ_4: 903.7 ns ± 123.5 ps	τ_1: -- τ_2: 1.481 ps ± 0.111 ps τ_3: 17.95 ps ± 3.536 ps τ_4: 946.0 ps ± 83.49 ps
Co(IV)	550[2] (fitted 625)	τ_1: < IRF τ_2: 10.39 ps ± 8.239 ps τ_3: 522.7 ps ± 246.6 ps τ_4: --	τ_1: < IRF τ_2: 1.535 ps ± 0.283 ps τ_3: 11.78 ps ± 5.787 ps τ_4: 1.021 ns ± 292.1 ps

[1] Reference 57. [2] Reference 35. Fitted decay lifetimes correspond to hot carrier formation (τ_1), carrier thermalization via lattice dissipation (τ_2), free carrier absorption and fast recombination (τ_3), lattice cooling and long-lived charge trap states (τ_4), References 34, 42, 64-68. τ_1 is within the IRF of the measurement.

following photoexcitation. Figure 6 shows implications for oxygen evolving reactions (OER) where the solvated O_2 is monitored during successive cyclic voltammograms with the set

the grey dotted line. As the electrochemical current decreases, the percent O_2 saturation increases rapidly followed by a secondary more gradual rise in solvated oxygen concentration that

remains at a constant value until the next increase in electrochemical current. We observe that O_2 release is a rate limiting step, and that O_2 is released on the reductive wave from presumably Co(IV) sites. A direct comparison of OER catalytic activity shows that CoBi performs slightly better than CoPi after three successive cyclic voltammograms with an O_2 reading of 19% as opposed to 17% although the CoBi anodic electrode exhibited a peak oxygen reading of 27%. Such results were reproduced with CoBi consistently outperforming CoPi in solvated oxygen trials. When correlated with the ultrafast electronic and structural properties of the material, we can infer qualitative trends that have implications for OER catalytic activity. Table 1 revisits the oxidation state assignments for the CoPi anodic electrode with fitted excited state decay lifetimes under ambient conditions (open circuit voltage, air) and under a high bias voltage (+1.3 V, aqueous electrolyte). It is evident that while there is a modest change in the decay lifetimes for the Co(III) state, both the Co(II) and Co(IV) states demonstrate the appearance of additional decay lifetimes with the application of an external bias voltage. These lifetimes are assigned to fast carrier recombination, lattice cooling, and the formation of long-lived charge trap states. Additionally, the Co(IV) state shows a pronounced decrease in the fast decay lifetimes corresponding to hot carrier formation and carrier thermalization via lattice dissipation. Table 2 also revisits oxidation state assignments for the CoBi anodic electrode that exhibits behavior different from that of the CoPi anodic electrode. Overall, the lifetimes for the Co(II), Co(III), and Co(IV) states are observed to decrease with the application of an external bias voltage with the exception of an increase in the decay lifetime for lattice cooling and long-lived charge trap states for both the Co(III) and drastically for the Co(IV) state. Notably, CoBi does not exhibit an intermediate lifetime in the Co(II) state under ambient conditions that corresponds to lattice dissipation dynamics; however, this t_2 lifetime grows in under +1.3 V bias voltage and contributes to 35.3% of the overall amplitude under electrolytic conditions. Likewise, the Co(III) fast decay lifetime τ_1 initially makes up 84.5% of the overall amplitude under ambient non-electrolytic conditions; however, under electrolytic conditions this decay pathway disappears. The Co(IV) fast decay lifetime also undergoes a noticeable change with a drastic decrease from ambient non-electrolytic conditions to aqueous electrolytic conditions under an applied voltage of +1.3 V. Taken together, we can infer that changes in long timescale dynamics namely free carrier absorption and fast recombination as well as lattice cooling and trap states are more pronounced in the CoPi anodic electrode when the material is redox poised. These longer timescale dynamics concern the Co(II) and Co(IV) sites more so than Co(III) sites. As with hematite,[37, 74] we observe that a positive voltage results in a change in the free carrier absorption that is more prevalent in CoPi than in the CoBi material due to a decrease in background electron density and a decrease in recombination dynamics with longer-lived photoholes. On the other hand, CoBi exhibits a pronounced change in fast decay lifetimes namely hot carrier formation and carrier thermalization via lattice dissipation when the material is likewise redox poised. Here, the most pronounced changes in CoBi on fast timescales occur within the Co(II) and Co(III) spectral regions with the appearance of an additional long-lived lifetime in the Co(IV) state that parallels the behavior observed in CoPi. We can also correlate these fast decay dynamics with CoBi's long-range order and relatively more O_h Co(III) sites that favor charge migration through interlayer material sheets resulting in a reduction of hole-trapping behavior. Because both CoPi and CoBi exhibit a pronounced increase in the Co(IV) trap state lifetime with the application of external bias voltage, we cannot assume that the trap states participate directly in catalysis or that this is the primary reason behind why CoBi performs OER slightly better than CoPi. Instead, we can surmise that the fast timescale dynamics (< 100 ps) could be linked to enhanced catalytic OER behavior that provides convenient pathways within the electronic structure landscape for inter-domain charge hopping and lattice relaxation following LMCT excitation. Such findings are also consistent with our transient XANES measurements that show cumulative photoreductive changes at 400 nm illumination followed by back-electron transfer that is both transient (100 ps) and also long-lived in the CoBi material with only mild changes in the CoPi material.

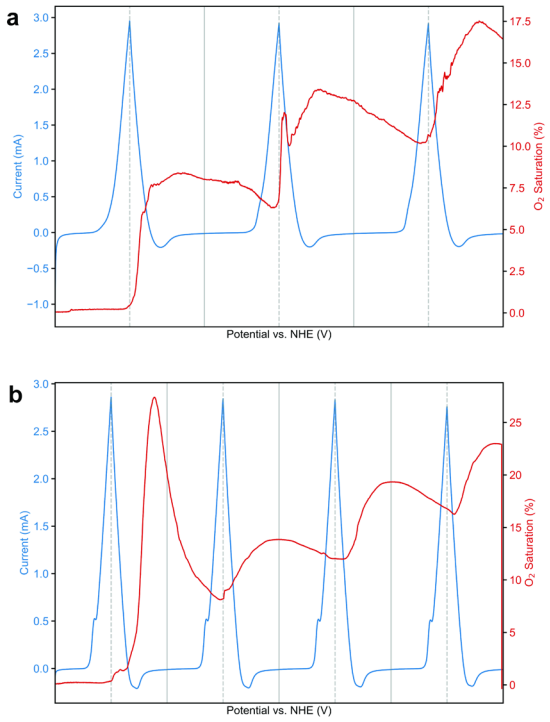

Figure 6. *In situ* electrochemical measurement of dissolved oxygen as a function of cyclic voltammogram scans between +0.71 V (solid vertical lines) to +1.51 V (vertical dotted lines) with an Ag/AgCl reference, Pt counter, and (a) CoPi anodic electrode in aqueous KPi electrolyte pH = 7.0 or (b) CoBi anodic electrode in aqueous KBi electrolyte pH = 9.0 with a scan rate of 5 mV/s.

In contrast to hematite and other crystalline photoanode materials, CoPi/CoBi consist of more disordered structures conferring greater sites for trap states with enhanced density and selectivity. Following oxidation, the photoanode surface becomes electron depleted. Whereas hematite contains trap states directly below the conduction band, our pump wavelength dependent TA results suggest the existence of deep trap states in the middle of the conduction-valence band gap that play a role in charge migration. These deep hole traps have been observed in other amorphous oxides such as silicon dioxide (SiO_2), aluminum oxide (Al_2O_3), and titanium dioxide (TiO_2).[76] When comparing the rate of rapid decay (Fig. 4c and 4d) within the first 5 ps, the pronounced difference in hot carrier formation and relaxation lifetimes can be correlated with the degree of structural disorder in the material. CoPi has a faster decay rate within the first 5 ps when compared with CoBi due to its small

domain size and relatively disordered long range material structure. This also leads to a higher density of trap states conferring faster lifetimes for nonradiative relaxation of hot carriers. Photoexcitation resonant to the band gap in semiconductors and metals has been known to induce band bending and photo-induced phase transitions that initially populate the conduction band leading to hole trapping at surface defect sites. The initial delocalization of charge occurs on timescales < 100 ps with localization of charge in surface defect states occurring on timescales of 200 ps or greater in metal oxides.[77, 78] Such observations can also aid in elucidating the transient XANES signal that consists of a significant non-thermal spectral signature where the 400 nm excitation in our studies is photoreductive and drives both electronic and thermal changes.

Our results are consistent with previous water oxidation studies on metal oxide photoanodes such as tungsten trioxide (WO_3), titanium dioxide (TiO_2), bismuth vanadate ($BiVO_4$), and hematite (α-Fe_2O_3).[15, 73, 79] Briefly, it has been proposed that high-energetic oxo species are directly linked to oxygen evolution reactions, and that kinetic models of these metal oxide photoanodes suggest competition between electron-hole recombination with long-lived holes, and that of the seconds to minutes timescales of water-splitting. More specifically, an increase by two orders of magnitude is observed in kinetic decay lifetimes when the photoanodes are oxidized from a set potential of +0.7 to +1.5 V (vs RHE) with the water-splitting reaction rate depending primarily on surface hole density.[15, 34, 37, 70-74, 79] This reinforces the importance of surface states and interlayer charge migration for facilitating water-splitting catalysis as previously observed with hematite and the photogenerated flux of holes needed to propagate through the bulk towards the surface or solid-liquid interface. The findings parallel oxygen evolution reactions in photosystem II where equilibrium is achieved through surface hole states and metal(OH)-O-metal(OH) sites and have far-reaching implications for water-splitting electrocatalytic and photo-electrocatalytic complexes in general.

CONCLUSIONS

We observe a net photoreduction reaction when CoPi and CoBi materials are excited with blue wavelengths (400 nm). Differing decay dynamics occur with varying degrees of dimensionality and charge delocalization due to inherent electronic and structural differences in the CoPi and CoBi anodic electrodes respectively. We observe that slightly increased dimensionality and greater charge delocalization within a 1D quantum confined layered structure leads to enhanced production of trapped charge carriers with reduced fast decay lifetimes corresponding to hot carriers and lattice dissipation dynamics that are a defining feature in CoBi. We note that such differences can have profound implications as a potential precursor state to water-splitting catalysis. Under redox poised conditions, we observe a potential dependence in the excited-state fraction of trapped charge carriers that is pump wavelength dependent suggestive of deep-trap states within the material and consistent with spectral signatures for the rapid decay in Co(IV) states predominantly on the 10 ps timescale leaving mostly Co(III) and Co(II) valency species. The observed reaction dynamics cannot be fully explained by photothermal effects alone, but rather are a combination of potentially competing or complementary processes that involve photoexcited charge transfer resonances, inter-domain electron hopping, and lattice relaxation dynamics as important features in the design of future water-splitting catalytic materials. The work has important applications for rationale design of water-splitting catalytic materials and considerations for electronic-structure relationships for photochemical redox activity.

ASSOCIATED CONTENT

Supporting Information. The Supporting Information is available free of charge.

Excited state fraction calculations, Ni K-edge transient XANES time-zero, SEM of electrodeposited thin films and colloidal suspensions, nanosecond transient absorption spectroscopy, steady-state XANES, In situ heating XAS at the Co K-edge, FEFF simulations of heating XAS measurements, femtosecond transient absorption of in situ electrochemical cell, optical spot size measurements, near-UV transient absorption spectroscopy, CoPi and CoBi excited state multiexponential decay analysis and kinetic fits under ambient open-circuit-voltage conditions and positive bias voltages.

AUTHOR INFORMATION

Corresponding Author

*** Lin X. Chen** – Department of Chemistry, Northwestern University, Evanston, IL 60201 USA; Division of Chemical Sciences & Engineering, Argonne National Laboratory, Lemont, IL 60439 USA; l-chen@northwestern.edu

Authors

Emily Sprague-Klein – Division of Chemical Sciences & Engineering, Argonne National Laboratory, Lemont, IL 60439 USA; Department of Chemistry, Northwestern University, Evanston, IL 60201 USA; emily_sprague-klein@brown.edu

Brian T. Phelan – Division of Chemical Sciences & Engineering, Argonne National Laboratory, Lemont, IL 60439 USA

Michael Mara – Division of Chemical Sciences & Engineering, Argonne National Laboratory, Lemont, IL 60439 USA; Department of Chemistry, Northwestern University, Evanston, IL 60201 USA; b83973@anl.gov

Jin Yu – X-ray Science Division, Argonne National Laboratory, Lemont IL 60439 USA.

Matthew Drummer – Department of Chemistry, University of Illinois at Chicago, IL 60607 USA.

Xiang He - Division of Chemical Sciences & Engineering, Argonne National Laboratory, Lemont, IL 60439 USA.

Ksenija Glusac – Department of Chemistry, University of Illinois at Chicago, IL 60607 USA; Division of Chemical Sciences & Engineering, Argonne National Laboratory, Lemont, IL 60439 USA.

Sungsik Lee – X-ray Science Division, Argonne National Laboratory, Lemont IL 60439 USA.

Benjamin Reinhart - X-ray Science Division, Argonne National Laboratory, Lemont IL 60439 USA.

Xiaoyi Zhang – X-ray Science Division, Argonne National Laboratory, Lemont IL 60439 USA.

David Tiede – Division of Chemical Sciences & Engineering, Argonne National Laboratory, Lemont, IL 60439 USA.

Present Addresses

Emily Sprague-Klein – Department of Chemistry, Brown University, Providence RI 02912

Brian T. Phelan – Paula M. Trienes Institute for Sustainability and Energy, Northwestern University, Evanston IL 60208

Jin Yu – KLA Corporation, Milpitas, CA 95036

Matthew Drummer – Department of Chemistry, Harvard University, Boston MA 02138

Xiang He – Department of Mechanical and Civil Engineering, Florida Institute of Technology, Melbourne, FL, 32901 USA

Author Contributions

E.S.K, D.T. and L.C conceived of the experiments; E.S.K. executed all optical/x-ray spectroscopy and imaging measurements, design of setups, sample preparation, alignment, and data analysis; B.P., M.M., J.Y., X.H. assisted in data acquisition. All authors have given approval to the final version of the manuscript.

ACKNOWLEDGMENT

We acknowledge funding from the U.S. Department of Energy, Office of Science, Office of Basic Energy Sciences, Solar Photochemistry Program within the Division of Chemical Sciences, Geosciences, and Biosciences, through Argonne National Laboratory under Contract No. DE-AC02-06CH11357. This research used beamlines 11-ID-D and 12-BM of the Advanced Photon Source, a U.S. Department of Energy (DOE) Office of Science user facility operated for the DOE Office of Science by Argonne National Laboratory under Contract No. DE-AC02-06CH11357. We also thank Dr. Magali Ferrandon and Dr. Ahmed Farghaly for the use of research instrumentation in the High-throughput Research Laboratory, and Dr. Alex Martinson for use of sputter deposition methods prior to imaging. We also acknowledge Educational Programs and Outreach at Argonne for the additional use of facilities related to imaging. We also thank the Solar Energy Conversion Group for interesting discussions.

ABBREVIATIONS

CoPi, Cobalt-Phosphate; CoBi, Cobalt-Borate; XAS, X-ray absorption spectroscopy; OER, oxygen evolution reaction; OEC, oxygen evolution catalyst; EXAFS, extended X-ray absorption fine structure; RIXS, resonant inelastic X-ray scattering; XANES, X-ray absorption near edge structure; KPi, potassium phosphate; KOH, potassium hydroxide; NHE, normal hydrogen electrode; ITO, indium tin oxide; XTA, X-ray transient absorption; DMF, dimethylformamide; APD, avalanche photodiode detector; LBO, lithium triborate; BBO, beta barium borate; SHG, second harmonic generation; IRF, instrument response function; TA, transient absorption spectroscopy; SEM, scanning electron microscopy; LMCT, ligand to metal charge transfer; MMCT, metal to metal charge transfer; OPG, optical parametric generator

REFERENCES

(1) Xie, C.; Niu, Z.; Kim, D.; Li, M.; Yang, P. Surface and Interface Control in Nanoparticle Catalysis. *Chemical Reviews* **2020**, *120* (2), 1184-1249. DOI: 10.1021/acs.chemrev.9b00220.
(2) Crisenza, G. E. M.; Melchiorre, P. Chemistry glows green with photoredox catalysis. *Nature Communications* **2020**, *11* (1), 803. DOI: 10.1038/s41467-019-13887-8.
(3) Qin, R.; Liu, K.; Wu, Q.; Zheng, N. Surface Coordination Chemistry of Atomically Dispersed Metal Catalysts. *Chemical Reviews* **2020**, *120* (21), 11810-11899. DOI: 10.1021/acs.chemrev.0c00094.
(4) Chen, L.; Msigwa, G.; Yang, M.; Osman, A. I.; Fawzy, S.; Rooney, D. W.; Yap, P.-S. Strategies to achieve a carbon neutral society: a review. *Environmental Chemistry Letters* **2022**, *20* (4), 2277-2310. DOI: 10.1007/s10311-022-01435-8.
(5) Chen, L. X. Organic Solar Cells: Recent Progress and Challenges. *ACS Energy Letters* **2019**, *4* (10), 2537-2539. DOI: 10.1021/acsenergylett.9b02071.
(6) Dalle, K. E.; Warnan, J.; Leung, J. J.; Reuillard, B.; Karmel, I. S.; Reisner, E. Electro- and Solar-Driven Fuel Synthesis with First Row Transition Metal Complexes. *Chemical Reviews* **2019**, *119* (4), 2752-2875. DOI: 10.1021/acs.chemrev.8b00392.
(7) Li, H.; Kelly, S.; Guevarra, D.; Wang, Z.; Wang, Y.; Haber, J. A.; Anand, M.; Gunasooriya, G. T. K. K.; Abraham, C. S.; Vijay, S.; et al. Analysis of the limitations in the oxygen reduction activity of transition metal oxide surfaces. *Nature Catalysis* **2021**, *4* (6), 463-468. DOI: 10.1038/s41929-021-00618-w.
(8) Zhou, K. L.; Wang, Z.; Han, C. B.; Ke, X.; Wang, C.; Jin, Y.; Zhang, Q.; Liu, J.; Wang, H.; Yan, H. Platinum single-atom catalyst coupled with transition metal/metal oxide heterostructure for accelerating alkaline hydrogen evolution reaction. *Nature Communications* **2021**, *12* (1), 3783. DOI: 10.1038/s41467-021-24079-8.
(9) Wang, J.; Kim, S.-J.; Liu, J.; Gao, Y.; Choi, S.; Han, J.; Shin, H.; Jo, S.; Kim, J.; Ciucci, F.; et al. Redirecting dynamic surface restructuring of a layered transition metal oxide catalyst for superior water oxidation. *Nature Catalysis* **2021**, *4* (3), 212-222. DOI: 10.1038/s41929-021-00578-1.
(10) Song, S.; Wu, Y.; Ge, S.; Wang, L.; Wang, Y.; Guo, Y.; Zhan, W.; Guo, Y. A Facile Way To Improve Pt Atom Efficiency for CO Oxidation at Low Temperature: Modification by Transition Metal Oxides. *ACS Catalysis* **2019**, *9* (7), 6177-6187. DOI: 10.1021/acscatal.9b01679.
(11) Hausmann, J. N.; Mebs, S.; Dau, H.; Driess, M.; Menezes, P. W. Oxygen Evolution Activity of Amorphous Cobalt Oxyhydroxides: Interconnecting Precatalyst Reconstruction, Long-Range Order, Buffer-Binding, Morphology, Mass Transport, and Operation Temperature. *Advanced Materials* **2022**, *34* (50), 2207494. DOI: https://doi.org/10.1002/adma.202207494.
(12) Chen, D.; Dong, C.-L.; Zou, Y.; Su, D.; Huang, Y.-C.; Tao, L.; Dou, S.; Shen, S.; Wang, S. In situ evolution of

highly dispersed amorphous CoOx clusters for oxygen evolution reaction. *Nanoscale* **2017**, *9* (33), 11969-11975, 10.1039/C7NR04381C. DOI: 10.1039/C7NR04381C.
(13) Gong, L.; Chng, X. Y. E.; Du, Y.; Xi, S.; Yeo, B. S. Enhanced Catalysis of the Electrochemical Oxygen Evolution Reaction by Iron(III) Ions Adsorbed on Amorphous Cobalt Oxide. *ACS Catalysis* **2018**, *8* (2), 807-814. DOI: 10.1021/acscatal.7b03509.
(14) Anantharaj, S.; Reddy, P. N.; Kundu, S. Core-Oxidized Amorphous Cobalt Phosphide Nanostructures: An Advanced and Highly Efficient Oxygen Evolution Catalyst. *Inorganic Chemistry* **2017**, *56* (3), 1742-1756. DOI: 10.1021/acs.inorgchem.6b02929.
(15) Reith, L.; Triana, C. A.; Pazoki, F.; Amiri, M.; Nyman, M.; Patzke, G. R. Unraveling Nanoscale Cobalt Oxide Catalysts for the Oxygen Evolution Reaction: Maximum Performance, Minimum Effort. *Journal of the American Chemical Society* **2021**, *143* (37), 15022-15038. DOI: 10.1021/jacs.1c03375.
(16) Lee, S. A.; Lee, T. H.; Kim, C.; Choi, M.-J.; Park, H.; Choi, S.; Lee, J.; Oh, J.; Kim, S. Y.; Jang, H. W. Amorphous Cobalt Oxide Nanowalls as Catalyst and Protection Layers on n-Type Silicon for Efficient Photoelectrochemical Water Oxidation. *ACS Catalysis* **2020**, *10* (1), 420-429. DOI: 10.1021/acscatal.9b03899.
(17) Reddy, D. A.; Kim, Y.; Shim, H. S.; Reddy, K. A. J.; Gopannagari, M.; Praveen Kumar, D.; Song, J. K.; Kim, T. K. Significant Improvements on BiVO4@CoPi Photoanode Solar Water Splitting Performance by Extending Visible-Light Harvesting Capacity and Charge Carrier Transportation. *ACS Applied Energy Materials* **2020**, *3* (5), 4474-4483. DOI: 10.1021/acsaem.0c00169.
(18) Thorarinsdottir, A. E.; Veroneau, S. S.; Nocera, D. G. Self-healing oxygen evolution catalysts. *Nature Communications* **2022**, *13* (1), 1243. DOI: 10.1038/s41467-022-28723-9.
(19) Veroneau, S. S.; Nocera, D. G. Continuous electrochemical water splitting from natural water sources via forward osmosis. *Proceedings of the National Academy of Sciences* **2021**, *118* (9), e2024855118. DOI: doi:10.1073/pnas.2024855118.
(20) Barber, J. Solar-driven water-splitting provides a solution to the energy problem underpinning climate change. *Biochemical Society Transactions* **2020**, *48* (6), 2865-2874. DOI: 10.1042/bst20200758 (acccessed 9/14/2023).
(21) Yang, W.; Prabhakar, R. R.; Tan, J.; Tilley, S. D.; Moon, J. Strategies for enhancing the photocurrent, photovoltage, and stability of photoelectrodes for photoelectrochemical water splitting. *Chemical Society Reviews* **2019**, *48* (19), 4979-5015, 10.1039/C8CS00997J. DOI: 10.1039/C8CS00997J.
(22) Sprague-Klein, E. A.; He, X.; Mara, M. W.; Reinhart, B. J.; Lee, S.; Utschig, L. M.; Mulfort, K. L.; Chen, L. X.; Tiede, D. M. Photo-electrochemical Effect in the Amorphous Cobalt Oxide Water Oxidation Catalyst Cobalt–Phosphate (CoPi). *ACS Energy Letters* **2022**, *7* (9), 3129-3138. DOI: 10.1021/acsenergylett.2c01560.
(23) Kanan, M. W.; Yano, J.; Surendranath, Y.; Dincă, M.; Yachandra, V. K.; Nocera, D. G. Structure and Valency of a Cobalt−Phosphate Water Oxidation Catalyst Determined by in Situ X-ray Spectroscopy. *Journal of the American Chemical Society* **2010**, *132* (39), 13692-13701. DOI: 10.1021/ja1023767.
(24) Nocera, D. G. The Artificial Leaf. *Accounts of Chemical Research* **2012**, *45* (5), 767-776. DOI: 10.1021/ar2003013.
(25) Surendranath, Y.; Bediako, D. K.; Nocera, D. G. Interplay of oxygen-evolution kinetics and photovoltaic power curves on the construction of artificial leaves. *Proceedings of the National Academy of Sciences* **2012**, *109* (39), 15617. DOI: 10.1073/pnas.1118341109.
(26) Khnayzer, R. S.; Mara, M. W.; Huang, J.; Shelby, M. L.; Chen, L. X.; Castellano, F. N. Structure and Activity of Photochemically Deposited "CoPi" Oxygen Evolving Catalyst on Titania. *ACS Catalysis* **2012**, *2* (10), 2150-2160. DOI: 10.1021/cs3005192.
(27) Kwon, G.; Kokhan, O.; Han, A.; Chapman, K. W.; Chupas, P. J.; Du, P.; Tiede, D. M. Oxyanion induced variations in domain structure for amorphous cobalt oxide oxygen evolving catalysts, resolved by X-ray pair distribution function analysis. *Acta Crystallogr B Struct Sci Cryst Eng Mater* **2015**, *71* (Pt 6), 713-721. DOI: 10.1107/S2052520615022180 PubMed.
(28) Kwon, G.; Jang, H.; Lee, J.-S.; Mane, A.; Mandia, D. J.; Soltau, S. R.; Utschig, L. M.; Martinson, A. B. F.; Tiede, D. M.; Kim, H.; et al. Resolution of Electronic and Structural Factors Underlying Oxygen-Evolving Performance in Amorphous Cobalt Oxide Catalysts. *Journal of the American Chemical Society* **2018**, *140* (34), 10710-10720. DOI: 10.1021/jacs.8b02719.
(29) Keane, T. P.; Veroneau, S. S.; Hartnett, A. C.; Nocera, D. G. Generation of Pure Oxygen from Briny Water by Binary Catalysis. *Journal of the American Chemical Society* **2023**, *145* (9), 4989-4993. DOI: 10.1021/jacs.3c00176.
(30) Thomas, B.; Tang, C.; Ramírez-Hernández, M.; Asefa, T. Incorporation of Bismuth Increases the Electrocatalytic Activity of Cobalt Borates for Oxygen Evolution Reaction. *ChemPlusChem* **2023**, *88* (5), e202300104. DOI: https://doi.org/10.1002/cplu.202300104.
(31) Tiede, D. M.; Kim, T. W.; Sprague-Klein, E.; Kwon, G.; Martinson, A. B. F.; Mulfort, K. L. (Invited) Tracking Structures in Solar Fuels Catalysis: In-Situ X-Ray Structure Characterization of Interfacial Water-Splitting Molecular and Thin-Film Catalysts. *ECS Meeting Abstracts* **2019**, *MA2019-02* (41), 1955. DOI: 10.1149/MA2019-02/41/1955.
(32) Risch, M.; Khare, V.; Zaharieva, I.; Gerencser, L.; Chernev, P.; Dau, H. Cobalt−Oxo Core of a Water-Oxidizing Catalyst Film. *Journal of the American Chemical Society* **2009**, *131* (20), 6936-6937. DOI: 10.1021/ja902121f.
(33) Eom, C. J.; Suntivich, J. In Situ Stimulated Raman Spectroscopy Reveals the Phosphate Network in the Amorphous Cobalt Oxide Catalyst and Its Role in the Catalyst Formation. *The Journal of Physical Chemistry C* **2019**, *123* (48), 29284-29290. DOI: 10.1021/acs.jpcc.9b10308.

(34) Barroso, M.; Cowan, A. J.; Pendlebury, S. R.; Grätzel, M.; Klug, D. R.; Durrant, J. R. The Role of Cobalt Phosphate in Enhancing the Photocatalytic Activity of α-Fe2O3 toward Water Oxidation. *Journal of the American Chemical Society* **2011**, *133* (38), 14868-14871. DOI: 10.1021/ja205325v.
(35) Hadt, R. G.; Hayes, D.; Brodsky, C. N.; Ullman, A. M.; Casa, D. M.; Upton, M. H.; Nocera, D. G.; Chen, L. X. X-ray Spectroscopic Characterization of Co(IV) and Metal–Metal Interactions in Co4O4: Electronic Structure Contributions to the Formation of High-Valent States Relevant to the Oxygen Evolution Reaction. *Journal of the American Chemical Society* **2016**, *138* (34), 11017-11030. DOI: 10.1021/jacs.6b04663.
(36) Pasquini, C.; Liu, S.; Chernev, P.; Gonzalez-Flores, D.; Mohammadi, M. R.; Kubella, P.; Jiang, S.; Loos, S.; Klingan, K.; Sikolenko, V.; et al. Operando tracking of oxidation-state changes by coupling electrochemistry with time-resolved X-ray absorption spectroscopy demonstrated for water oxidation by a cobalt-based catalyst film. *Analytical and Bioanalytical Chemistry* **2021**, *413* (21), 5395-5408. DOI: 10.1007/s00216-021-03515-0.
(37) Pendlebury, S. R.; Barroso, M.; Cowan, A. J.; Sivula, K.; Tang, J.; Grätzel, M.; Klug, D.; Durrant, J. R. Dynamics of photogenerated holes in nanocrystalline α-Fe2O3 electrodes for water oxidation probed by transient absorption spectroscopy. *Chemical Communications* **2011**, *47* (2), 716-718, 10.1039/C0CC03627G. DOI: 10.1039/C0CC03627G.
(38) Burmeister, C. F.; Kwade, A. Process engineering with planetary ball mills. *Chemical Society Reviews* **2013**, *42* (18), 7660-7667, 10.1039/C3CS35455E. DOI: 10.1039/C3CS35455E.
(39) Šepelák, V.; Bégin-Colin, S.; Le Caër, G. Transformations in oxides induced by high-energy ball-milling. *Dalton Transactions* **2012**, *41* (39), 11927-11948, 10.1039/C2DT30349C. DOI: 10.1039/C2DT30349C.
(40) Weeber, A. W.; Bakker, H. Amorphization by ball milling. A review. *Physica B: Condensed Matter* **1988**, *153* (1), 93-135. DOI: https://doi.org/10.1016/0921-4526(88)90038-5.
(41) Chen, L. X.; Zhang, X. Photochemical Processes Revealed by X-ray Transient Absorption Spectroscopy. *The Journal of Physical Chemistry Letters* **2013**, *4* (22), 4000-4013. DOI: 10.1021/jz401750g.
(42) Chen, L. X.; Zhang, X.; Wasinger, E. C.; Attenkofer, K.; Jennings, G.; Muresan, A. Z.; Lindsey, J. S. Tracking Electrons and Atoms in a Photoexcited Metalloporphyrin by X-ray Transient Absorption Spectroscopy. *Journal of the American Chemical Society* **2007**, *129* (31), 9616-9618. DOI: 10.1021/ja072979v.
(43) Phelan, B. T.; Mara, M. W.; Chen, L. X. Excited-state structural dynamics of nickel complexes probed by optical and X-ray transient absorption spectroscopies: insights and implications. *Chemical Communications* **2021**, *57* (90), 11904-11921, 10.1039/D1CC03875C. DOI: 10.1039/D1CC03875C.
(44) Hayes, D.; Hadt, R. G.; Emery, J. D.; Cordones, A. A.; Martinson, A. B. F.; Shelby, M. L.; Fransted, K. A.; Dahlberg, P. D.; Hong, J.; Zhang, X.; et al. Electronic and nuclear contributions to time-resolved optical and X-ray absorption spectra of hematite and insights into photoelectrochemical performance. *Energy & Environmental Science* **2016**, *9* (12), 3754-3769, 10.1039/C6EE02266A. DOI: 10.1039/C6EE02266A.
(45) Kinigstein, E. D.; Jennings, G.; Kurtz, C. A.; March, A. M.; Zuo, X.; Chen, L. X.; Attenkofer, K.; Zhang, X. X-ray multi-probe data acquisition: A novel technique for laser pump x-ray transient absorption spectroscopy. *Review of Scientific Instruments* **2021**, *92* (8). DOI: 10.1063/5.0050713 (acccessed 6/19/2024).
(46) Kramar, B. V.; Phelan, B. T.; Sprague-Klein, E. A.; Diroll, B. T.; Lee, S.; Otake, K.-i.; Palmer, R.; Mara, M. W.; Farha, O. K.; Hupp, J. T.; et al. Single-Atom Metal Oxide Sites as Traps for Charge Separation in the Zirconium-Based Metal–Organic Framework NDC–NU-1000. *Energy & Fuels* **2021**, *35* (23), 19081-19095. DOI: 10.1021/acs.energyfuels.1c02623.
(47) Sprague-Klein, E. A.; Ho-Wu, R.; Nguyen, D.; Coste, S. C.; Wu, Y.; McMahon, J. J.; Seideman, T.; Schatz, G. C.; Van Duyne, R. P. Modulating the Electron Affinity of Small Bipyridyl Molecules on Single Gold Nanoparticles for Plasmon-Driven Electron Transfer. *The Journal of Physical Chemistry C* **2021**, *125* (40), 22142-22153. DOI: 10.1021/acs.jpcc.1c07803.
(48) Ravel, B.; Newville, M. ATHENA, ARTEMIS, HEPHAESTUS: data analysis for X-ray absorption spectroscopy using IFEFFIT. *J Synchrotron Radiat* **2005**, *12* (Pt 4), 537-541. DOI: 10.1107/s0909049505012719 From NLM.
(49) Brodsky, C. N.; Hadt, R. G.; Hayes, D.; Reinhart, B. J.; Li, N.; Chen, L. X.; Nocera, D. G. In situ characterization of cofacial Co(IV) centers in Co₄O₄ cubane: Modeling the high-valent active site in oxygen-evolving catalysts. *Proceedings of the National Academy of Sciences* **2017**, *114* (15), 3855-3860. DOI: doi:10.1073/pnas.1701816114.
(50) Hayes, D.; Kohler, L.; Hadt, R. G.; Zhang, X.; Liu, C.; Mulfort, Karen L.; Chen, L. X. Excited state electron and energy relays in supramolecular dinuclear complexes revealed by ultrafast optical and X-ray transient absorption spectroscopy. *Chemical Science* **2018**, *9* (4), 860-875, 10.1039/C7SC04055E. DOI: 10.1039/C7SC04055E.
(51) Wang, L.; Xie, Z.-L.; Phelan, B. T.; Lynch, V. M.; Chen, L. X.; Mulfort, K. L. Changing Directions: Influence of Ligand Electronics on the Directionality and Kinetics of Photoinduced Charge Transfer in Cu(I)Diimine Complexes. *Inorganic Chemistry* **2023**, *62* (35), 14368-14376. DOI: 10.1021/acs.inorgchem.3c02043.
(52) Gimeno, L.; Phelan, B. T.; Sprague-Klein, E. A.; Roisnel, T.; Blart, E.; Gourlaouen, C.; Chen, L. X.; Pellegrin, Y. Bulky and Stable Copper(I)-Phenanthroline Complex: Impact of Steric Strain and Symmetry on the Excited-State Properties. *Inorganic Chemistry* **2022**, *61* (19), 7296-7307. DOI: 10.1021/acs.inorgchem.1c03901.
(53) Potocny, A. M.; Phelan, B. T.; Sprague-Klein, E. A.; Mara, M. W.; Tiede, D. M.; Chen, L. X.; Mulfort, K. L. Harnessing Intermolecular Interactions to Promote Long-Lived Photoinduced Charge Separation from Copper Phenanthroline Chromophores. *Inorganic Chemistry* **2022**,

61 (48), 19119-19133. DOI: 10.1021/acs.inorgchem.2c02648.
(54) Greenfield, S. R.; Wasielewski, M. R. Near-transform-limited visible and near-IR femtosecond pulses from optical parametric amplification using Type II β-barium borate. *Opt. Lett.* **1995**, *20* (12), 1394-1396. DOI: 10.1364/OL.20.001394.
(55) Wang, L.; Williams, N. E.; Malachosky, E. W.; Otto, J. P.; Hayes, D.; Wood, R. E.; Guyot-Sionnest, P.; Engel, G. S. Scalable Ligand-Mediated Transport Synthesis of Organic–Inorganic Hybrid Perovskite Nanocrystals with Resolved Electronic Structure and Ultrafast Dynamics. *ACS Nano* **2017**, *11* (3), 2689-2696. DOI: 10.1021/acsnano.6b07574.
(56) Drummer, M. C.; Weerasooriya, R. B.; Gupta, N.; Askins, E. J.; Liu, X.; Valentine, A. J. S.; Li, X.; Glusac, K. D. Proton-Coupled Electron Transfer in a Ruthenium(II) Bipyrimidine Complex in Its Ground and Excited Electronic States. *The Journal of Physical Chemistry A* **2022**, *126* (27), 4349-4358. DOI: 10.1021/acs.jpca.2c02255.
(57) Weerasooriya, R. B.; Drummer, M. C.; Phelan, B. T.; Gesiorski, J. L.; Sprague-Klein, E. A.; Chen, L. X.; Glusac, K. D. Toward Metal-free Photocatalysis: Photochemical Regeneration of Organic Hydride Donors Using Phenazine-Based Photosensitizers. *The Journal of Physical Chemistry C* **2022**, *126* (42), 17816-17825. DOI: 10.1021/acs.jpcc.2c03541.
(58) Baker, L. R.; Jiang, C.-M.; Kelly, S. T.; Lucas, J. M.; Vura-Weis, J.; Gilles, M. K.; Alivisatos, A. P.; Leone, S. R. Charge Carrier Dynamics of Photoexcited Co3O4 in Methanol: Extending High Harmonic Transient Absorption Spectroscopy to Liquid Environments. *Nano Letters* **2014**, *14* (10), 5883-5890. DOI: 10.1021/nl502817a.
(59) Jiang, C.-M.; Baker, L. R.; Lucas, J. M.; Vura-Weis, J.; Alivisatos, A. P.; Leone, S. R. Characterization of Photo-Induced Charge Transfer and Hot Carrier Relaxation Pathways in Spinel Cobalt Oxide (Co3O4). *The Journal of Physical Chemistry C* **2014**, *118* (39), 22774-22784. DOI: 10.1021/jp5071133.
(60) Biswas, S.; Husek, J.; Londo, S.; Baker, L. R. Highly Localized Charge Transfer Excitons in Metal Oxide Semiconductors. *Nano Letters* **2018**, *18* (2), 1228-1233. DOI: 10.1021/acs.nanolett.7b04818.
(61) Klingan, K.; Ringleb, F.; Zaharieva, I.; Heidkamp, J.; Chernev, P.; Gonzalez-Flores, D.; Risch, M.; Fischer, A.; Dau, H. Water Oxidation by Amorphous Cobalt-Based Oxides: Volume Activity and Proton Transfer to Electrolyte Bases. *ChemSusChem* **2014**, *7* (5), 1301-1310. DOI: https://doi.org/10.1002/cssc.201301019.
(62) Farrow, C. L.; Bediako, D. K.; Surendranath, Y.; Nocera, D. G.; Billinge, S. J. L. Intermediate-Range Structure of Self-Assembled Cobalt-Based Oxygen-Evolving Catalyst. *Journal of the American Chemical Society* **2013**, *135* (17), 6403-6406. DOI: 10.1021/ja401276f.
(63) Mirzoyan, R.; Follmer, A. H.; Hadt, R. G. Observing Long-Lived Photogenerated Holes in Cobalt Oxyhydroxide Oxygen Evolution Catalysts. *ACS Applied Energy Materials* **2024**, *7* (7), 2837-2846. DOI: 10.1021/acsaem.3c03269.
(64) Mahl, J.; Neppl, S.; Roth, F.; Borgwardt, M.; Saladrigas, C.; Toulson, B.; Cooper, J.; Rahman, T.; Bluhm, H.; Guo, J.; et al. Decomposing electronic and lattice contributions in optical pump – X-ray probe transient inner-shell absorption spectroscopy of CuO. *Faraday Discussions* **2019**, *216* (0), 414-433, 10.1039/C8FD00236C. DOI: 10.1039/C8FD00236C.
(65) Su, H.; Xu, Y.-F.; Feng, S.-C.; Wu, Z.-G.; Sun, X.-P.; Shen, C.-H.; Wang, J.-Q.; Li, J.-T.; Huang, L.; Sun, S.-G. Hierarchical Mn2O3 Hollow Microspheres as Anode Material of Lithium Ion Battery and Its Conversion Reaction Mechanism Investigated by XANES. *ACS Applied Materials & Interfaces* **2015**, *7* (16), 8488-8494. DOI: 10.1021/am509198k.
(66) Costentin, C.; Porter, T. R.; Savéant, J.-M. Conduction and Reactivity in Heterogeneous-Molecular Catalysis: New Insights in Water Oxidation Catalysis by Phosphate Cobalt Oxide Films. *Journal of the American Chemical Society* **2016**, *138* (17), 5615-5622. DOI: 10.1021/jacs.6b00737.
(67) González-Flores, D.; Sánchez, I.; Zaharieva, I.; Klingan, K.; Heidkamp, J.; Chernev, P.; Menezes, P. W.; Driess, M.; Dau, H.; Montero, M. L. Heterogeneous Water Oxidation: Surface Activity versus Amorphization Activation in Cobalt Phosphate Catalysts. *Angewandte Chemie International Edition* **2015**, *54* (8), 2472-2476. DOI: https://doi.org/10.1002/anie.201409333.
(68) Eberhart, M. S.; Phelan, B. T.; Niklas, J.; Sprague-Klein, E. A.; Kaphan, D. M.; Gosztola, D. J.; Chen, L. X.; Tiede, D. M.; Poluektov, O. G.; Mulfort, K. L. Surface immobilized copper(i) diimine photosensitizers as molecular probes for elucidating the effects of confinement at interfaces for solar energy conversion. *Chemical Communications* **2020**, *56* (81), 12130-12133, 10.1039/D0CC05972B. DOI: 10.1039/D0CC05972B.
(69) Negru, B.; McAnally, M. O.; Mayhew, H. E.; Ueltschi, T. W.; Peng, L.; Sprague-Klein, E. A.; Schatz, G. C.; Van Duyne, R. P. Fabrication of Gold Nanosphere Oligomers for Surface-Enhanced Femtosecond Stimulated Raman Spectroscopy. *The Journal of Physical Chemistry C* **2017**, *121* (48), 27004-27008. DOI: 10.1021/acs.jpcc.7b09664.
(70) Barroso, M.; Pendlebury, S. R.; Cowan, A. J.; Durrant, J. R. Charge carrier trapping, recombination and transfer in hematite (α-Fe2O3) water splitting photoanodes. *Chemical Science* **2013**, *4* (7), 2724-2734, 10.1039/C3SC50496D. DOI: 10.1039/C3SC50496D.
(71) Le Formal, F.; Pastor, E.; Tilley, S. D.; Mesa, C. A.; Pendlebury, S. R.; Grätzel, M.; Durrant, J. R. Rate Law Analysis of Water Oxidation on a Hematite Surface. *Journal of the American Chemical Society* **2015**, *137* (20), 6629-6637. DOI: 10.1021/jacs.5b02576.
(72) Mesa, C. A.; Francàs, L.; Yang, K. R.; Garrido-Barros, P.; Pastor, E.; Ma, Y.; Kafizas, A.; Rosser, T. E.; Mayer, M. T.; Reisner, E.; et al. Multihole water oxidation catalysis on haematite photoanodes revealed by operando spectroelectrochemistry and DFT. *Nature Chemistry* **2020**, *12* (1), 82-89. DOI: 10.1038/s41557-019-0347-1.

(73) Li, J.; Chen, H.; Triana, C. A.; Patzke, G. R. Hematite Photoanodes for Water Oxidation: Electronic Transitions, Carrier Dynamics, and Surface Energetics. *Angewandte Chemie International Edition* **2021**, *60* (34), 18380-18396. DOI: https://doi.org/10.1002/anie.202101783.
(74) Pendlebury, S. R.; Wang, X.; Le Formal, F.; Cornuz, M.; Kafizas, A.; Tilley, S. D.; Grätzel, M.; Durrant, J. R. Ultrafast Charge Carrier Recombination and Trapping in Hematite Photoanodes under Applied Bias. *Journal of the American Chemical Society* **2014**, *136* (28), 9854-9857. DOI: 10.1021/ja504473e.
(75) Chen, X.; Aschaffenburg, D. J.; Cuk, T. Selecting between two transition states by which water oxidation intermediates decay on an oxide surface. *Nature Catalysis* **2019**, *2* (9), 820-827. DOI: 10.1038/s41929-019-0332-5.
(76) Strand, J.; Kaviani, M.; Gao, D.; El-Sayed, A.-M.; Afanas'ev, V. V.; Shluger, A. L. Intrinsic charge trapping in amorphous oxide films: status and challenges. *Journal of Physics: Condensed Matter* **2018**, *30* (23), 233001. DOI: 10.1088/1361-648X/aac005.
(77) Gierster, L.; Vempati, S.; Stähler, J. Ultrafast generation and decay of a surface metal. *Nature Communications* **2021**, *12* (1), 978. DOI: 10.1038/s41467-021-21203-6.
(78) Calati, S.; Li, Q.; Zhu, X.; Stähler, J. Correction: Ultrafast evolution of the complex dielectric function of monolayer WS2 after photoexcitation. *Physical Chemistry Chemical Physics* **2021**, *23* (43), 24943-24943, 10.1039/D1CP90219A. DOI: 10.1039/D1CP90219A.
(79) Li, J.; Wan, W.; Triana, C. A.; Chen, H.; Zhao, Y.; Mavrokefalos, C. K.; Patzke, G. R. Reaction kinetics and interplay of two different surface states on hematite photoanodes for water oxidation. *Nature Communications* **2021**, *12* (1), 255. DOI: 10.1038/s41467-020-20510-8.

Authors are required to submit a graphic entry for the Table of Contents (TOC) that, in conjunction with the manuscript title, should give the reader a representative idea of one of the following: A key structure, reaction, equation, concept, or theorem, etc., that is discussed in the manuscript. Consult the journal's Instructions for Authors for TOC graphic specifications.

Insert Table of Contents artwork here